A Novel Sensorless Position and Speed Estimation Method for Heteropolar Inductor Machines

Jingzhe Wu, Martin J Balchin
University of Bath
Claverton Down, Bath, UK
E-Mail: j.wu2@bath.ac.uk, m.j.balchin@bath.ac.uk
http://www.bath.ac.uk

Keywords

«AC machine», «Motion control», «Sensorless control», «Controllers»

Abstract

This paper proposes a novel position/speed estimation method for a special type of armature side excited synchronous machine, namely heteropolar inductor machines, by taking advantage of the machines' unique structural characteristics. The field winding characteristics of heteropolar inductor machines are analyzed firstly. Analytical approaches for developing q-axis position and rotor speed estimation algorithm are then discussed, based only on terminal voltage and current measurements. Finally the validity of theories is supported by practical experiments, and the performance of estimations of position and speed under both steady state and transient conditions are shown by experiments in a prototype machine.

Introduction

Figure1 is a cross section view of a heteropolar inductor machine with 36 stator slots and 4 rotor saliencies. It is seen that all the windings are placed on the stator side and the rotor is completely passive. The three phase armature windings (denoted as A, B and C) are fed by balanced three phase AC, while the three sets of field windings (denoted as F_1, F_2 and F_3) are connected in series and fed by DC. The rotor shape ensures that only invariant and fundamental air gap permeance components (i.e. Λ_0 and Λ_1 respectively) are exhibited by rotor surface, as shown in Fig. 2. Such a machine structure is similar to that of flux switching machines [1, 2]. The theory of heteropolar inductor machines is analyzed in [3] based on space vector theories.

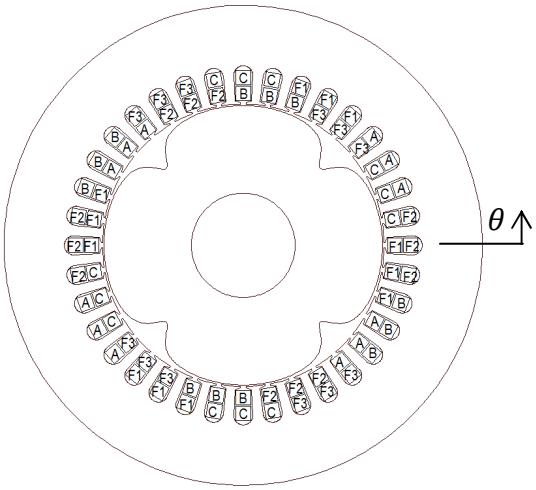

Fig. 1

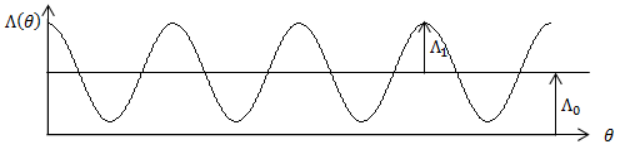

Fig. 2

Fig. 1: Cross section view of a 36 stator slots 4 rotor saliencies heteropolar inductor machine

Fig. 2: Air gap permeance variation

Sensorless position and speed estimation are extremely advantageous for modern sophisticated control strategies, e.g. field oriented control (FOC) [4] and direct torque control (DTC) [5], especially when measuring devices are not applicable. However the potential sensorless control schemes for heteropolar inductor machines are not extensively studied. On the other hand, certain sensorless estimation techniques developed for flux switching machines [6-8] can be applied for heteropolar inductor machines due to machine similarities. Nevertheless the methods are all based on flux linkage estimations, and will inevitable require terminal voltage integration, which may compromise the system performance due to potential integrator drift errors.

This paper introduces a novel sensorless q-axis and rotor speed estimation algorithm specialized on heteropolar inductor machines, by taking advantage of their unique structural characteristics. The proposed estimation method does not require any external signal injection, and is free from integrations and consequent potential drift errors.

Field Characteristics

The function of field windings in heteropolar inductor machines is to create an alternately reversed flux distribution along the air gap circumference. The spatial distribution of three field windings, as shown in Fig.1, is exactly the same as that of the armature windings. Each field winding axis is 120° apart in space from each other. However, the field windings are inter-connected in series instead of star connection as armature windings. The winding connections are sketched in Fig. 3. The field supply voltage and current are denoted as u_f and i_f respectively.

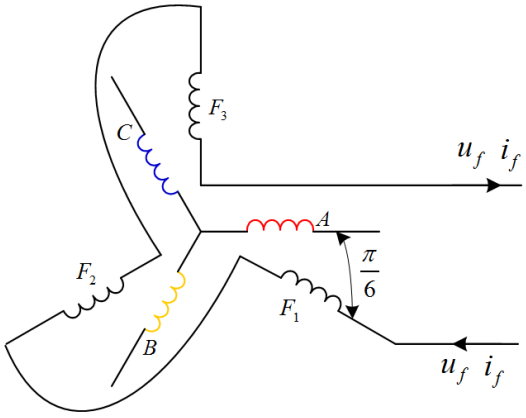

Fig. 3: Sketch of winding connections

The rotor rotation and armature reaction will cause flux variation in each field winding, and hence result in voltage variations. The flux linkage mathematical expressions for each field winding are developed in [3], and are expressed as

$$\lambda_{f1} = L_{lf} i_f + \frac{\pi}{6} N_f^2 i_f r\Lambda_0 + \frac{\sqrt{3}}{16} N_f^2 r\Lambda_1 \left(\bar{i}_f e^{-j\frac{\pi}{6}} + \bar{i}_f^* e^{j\frac{\pi}{6}} \right) + \frac{1}{4} k_{dp1} N_S N_f r\Lambda_0 \left(\bar{i}_S e^{-j\frac{\pi}{6}} + \bar{i}_S^* e^{j\frac{\pi}{6}} \right) \quad (1)$$

$$\lambda_{f2} = L_{lf} i_f + \frac{\pi}{6} N_f^2 i_f r\Lambda_0 + \frac{\sqrt{3}}{16} N_f^2 r\Lambda_1 \left(\bar{i}_f e^{-j\frac{5\pi}{6}} + \bar{i}_f^* e^{j\frac{5\pi}{6}} \right) + \frac{1}{4} k_{dp1} N_S N_f r\Lambda_0 \left(\bar{i}_S e^{-j\frac{5\pi}{6}} + \bar{i}_S^* e^{j\frac{5\pi}{6}} \right) \quad (2)$$

$$\lambda_{f3} = L_{lf} i_f + \frac{\pi}{6} N_f^2 i_f r\Lambda_0 + \frac{\sqrt{3}}{16} N_f^2 r\Lambda_1 \left(\bar{i}_f e^{j\frac{\pi}{2}} + \bar{i}_f^* e^{-j\frac{\pi}{2}} \right) + \frac{1}{4} k_{dp1} N_S N_f r\Lambda_0 \left(\bar{i}_S e^{j\frac{\pi}{2}} + \bar{i}_S^* e^{-j\frac{\pi}{2}} \right) \quad (3)$$

Numbers of winding turns of armature and field windings are denoted as N_S and N_f respectively.

The equations are written in space vector form, and $\bar{i}_f$ and $\bar{i}_S$ denote field current and armature current

vectors respectively. The space vectors are assumed to rotate in a stationary complex plane whose real axis is aligned to phase A axis. The machine bore radius is r. Field circuit leakage inductance is L_{lf}. The factor k_{dp1} is the fundamental winding factor.

As seen from (1-3), the varying components of field winding flux linkages are caused by both field excitation and armature reaction, and are balanced in 'three phases'. Varying flux linkages also induce AC voltages in field windings. Phase A voltage and field winding F_1 voltage are compared in Fig. 4, when the armature windings are supplied by switch mode power source. However the complete field circuit does not exhibit any varying voltages since the summation of λ_{f1}, λ_{f2} and λ_{f3} is 0.

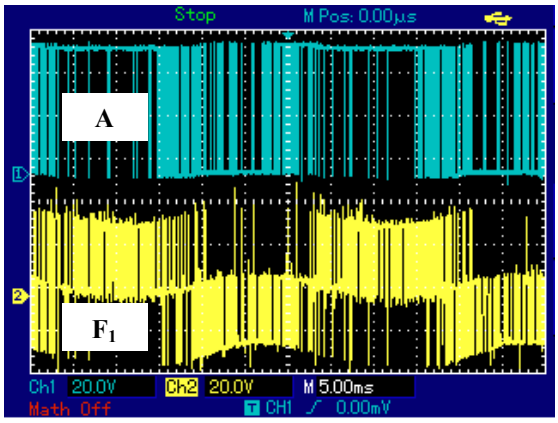

Fig. 4: Voltage waveforms of A and F_1 windings

It is possible to extract the q-axis position information from the field winding induced voltages, with the aid of phase terminal voltage measurements. It is discussed in detail in the next section.

Sensorless Estimation Algorithm

Even though the flux linkages of field windings show a pattern of three phase distribution, no space vector is generated for field flux linkage due to the series-connected field windings. However it is mathematically feasible to form a 'fictitious space vector' from field windings flux linkages,

$$\bar{\lambda}_f = \lambda_{f1} + \lambda_{f2} e^{j\frac{2\pi}{3}} + \lambda_{f3} e^{-j\frac{2\pi}{3}} = \frac{3}{4} k_{dp1} N_S N_f r \Lambda_0 \bar{i}_S \cdot e^{-j\frac{\pi}{6}} + \frac{3\sqrt{3}}{16} N_f^2 r \Lambda_1 \bar{i}_f \cdot e^{-j\frac{\pi}{6}} \tag{4}$$

Both the leakage field leakage flux linkage term and the time-invariant main flux linkage term are balanced out during formation of space vector $\overrightarrow{\lambda_f}$.

AC voltage components are induced in each of the field windings due to flux linkage variation, as shown in Fig. 4. The AC voltages of 'three phase' field windings are denoted as $\widetilde{u_{f1}}$, $\widetilde{u_{f2}}$ and $\widetilde{u_{f3}}$ and can be directly measured. Similarly a fictitious voltage space vector can be mathematically formed as

$$\bar{\tilde{u}}_f = \tilde{u}_{f1} + \tilde{u}_{f2} e^{j\frac{2\pi}{3}} + \tilde{u}_{f3} e^{j\frac{2\pi}{3}} \tag{5}$$

Also,

$$\bar{\tilde{u}}_f = \frac{d}{dt}\bar{\lambda}_f = \frac{d}{dt}\left(\frac{3}{4} k_{dp1} N_S N_f r \Lambda_0 \bar{i}_S \cdot e^{-j\frac{\pi}{6}}\right) + \frac{d}{dt}\left(\frac{3\sqrt{3}}{16} N_f^2 r \Lambda_1 \bar{i}_f \cdot e^{-j\frac{\pi}{6}}\right) \tag{6}$$

It is seen that both terms in (6) have a phase lag of π/6, and it can be eliminated to shift $\bar{\tilde{u}}_f$ by π/6 and obtain a new space vector $\bar{\tilde{u}}_f'$ as in (7). Such a phase shift requires purely complex number arithmetic, which can be processed within a micro-processer.

$$\bar{\tilde{u}}_f' = \bar{\tilde{u}}_f e^{j\frac{\pi}{6}} = \frac{d}{dt}\bar{\lambda}_f = \frac{d}{dt}\left(\frac{3}{4}k_{dp1}N_S N_f r\Lambda_0 \bar{i}_S\right) + \frac{d}{dt}\left(\frac{3\sqrt{3}}{16}N_f^2 r\Lambda_1 \bar{i}_f\right) \tag{7}$$

The mathematical expression of the armature voltage space vector can be formed by three phase armature voltage measurements in a similar way, and is developed in [3], hence

$$\vec{u}_S = u_{S1} + u_{S2}e^{j\frac{2\pi}{3}} + u_{S3}e^{j\frac{2\pi}{3}} \tag{8}$$

Also,

$$\vec{u}_S = \bar{i}_S R_S + \frac{d}{dt}\left(\frac{3}{4}k_{dp1}N_S^2 r\Lambda_0 \bar{i}_S\right) + \frac{d}{dt}\left(\frac{9}{16}N_S N_f r\Lambda_1 \bar{i}_f\right) \tag{9}$$

The leakage flux linkage term is eliminated in (9) since it only contributes a small portion to total armature winding flux linkages. The first term is a result of armature reaction while the second term results from field current excitation. Therefore the internal emf space vector $\vec{e}_S$ is

$$\vec{e}_S = \frac{d}{dt}\left(\frac{9}{16}N_S N_f r\Lambda_1 \bar{i}_f\right) = e_S \cdot e^{j\rho} \tag{10}$$

The spatial position of $\vec{e}_S$ is along the q-axis since the field current space vector is regarded as the d-axis. The angle ρ is the angle that the q-axis is displaced from the reference axis.

The number of turns of each coil shown in Fig.1 is the same, and therefore the total number of turns of both field and armature windings are equal. Hence

$$N_S = N_f \tag{11}$$

Subtracting (9) from (7), and substituting (10) and (11), gives

$$\vec{u}_S - \bar{\tilde{u}}_f = \bar{i}_S R_S + \left(1 - \frac{\sqrt{3}}{3}\right)\vec{e}_S \tag{12}$$

All the space vectors in (12) can be decomposed orthogonally to the reference plane by Clarke's Transform. The results of decomposition are re-arranged to calculate internal emf terms.

$$e_{S\alpha} = \frac{u_{S\alpha} - \tilde{u}_{f\alpha}' - i_{S\alpha}R_S}{1 - \frac{\sqrt{3}}{3}} \tag{13}$$

$$e_{S\beta} = \frac{u_{S\beta} - \tilde{u}_{f\beta}' - i_{S\beta}R_S}{1 - \frac{\sqrt{3}}{3}} \tag{14}$$

Quantities subscripted with α are the vectorial projections on phase A axis (α-axis), while the quantities subscripted with β are the vectorial projections on the orthogonal axis (β-axis). In the case

of large scale electrical machines, in which the winding resistance is low, the armature current terms can be discarded.

Equations (13) and (14) manage to estimate the orthogonal components of the internal emf space vector via measurable terminal quantities (i.e. voltages, currents). The location of q-axis ρ, therefore, is obtained by performing inverse trigonometric algorithm.

$$\rho = \begin{cases} \arcsin\left(\dfrac{e_{S\beta}}{\sqrt{e_{S\alpha}^2 + e_{S\beta}^2}}\right) & e_{S\alpha} \geq 0 \\ \pi - \arcsin\left(\dfrac{e_{S\beta}}{\sqrt{e_{S\alpha}^2 + e_{S\beta}^2}}\right) & e_{S\beta} < 0 \end{cases} \tag{15}$$

The waveforms of estimated quantities $e_{S\alpha}$ and $e_{S\beta}$ are plotted in Fig. 5 with zero-crossing points emphasised. $e_{S\alpha}$ and $e_{S\beta}$ are assumed to have constant amplitude and frequency.

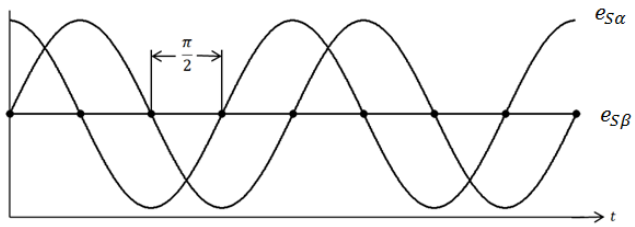

Fig. 5: Waveforms of $e_{S\alpha}$ and $e_{S\beta}$ and zero crossings

Since $e_{S\alpha}$ and $e_{S\beta}$ are orthogonal quantities, they cross zero points alternately. Hence the separation of each zero-crossing marked in Fig. 5 is π/2 in electrical radian. The average electrical speed between adjacent zero-crossings is thus estimated given the total time elapsed. The rotor mechanical speed, as suggested by the machine theory[9], is 1/4 of the electrical speed. This speed estimation method provides 16 speed updates per rotor revolution. This will generally meet the speed control purposes if the precision of speed sensing is not highly demanded. The estimated speed trajectory is in a step form, and a filter is applied to smoothen it.

The overall block diagram of the sensorless position/speed estimation scheme discussed is shown in Fig. 6.

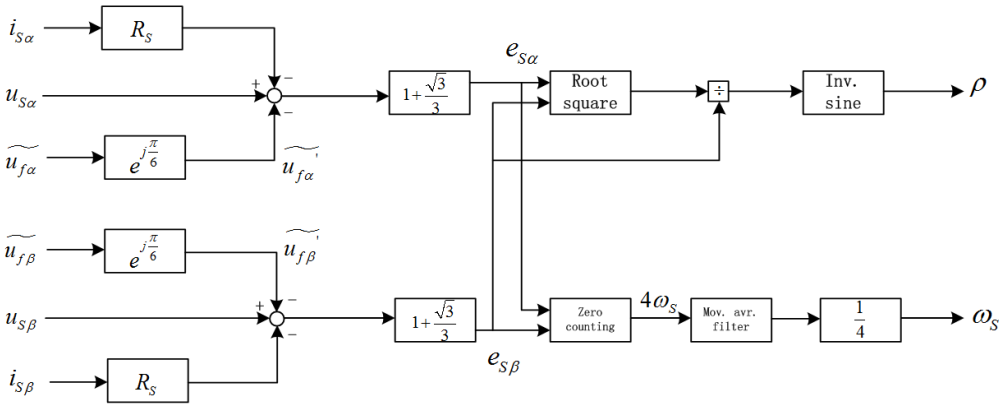

Fig. 6: Block diagram of sensorless q-axis position and rotor speed estimation

Experimental Verifications

The sensorless estimation method discussed is programmed in a micro-controller which has an interrupt rate of 10 kHz. A complete drive system, as shown in Fig. 7, is implemented to perform the practical experiments. Both steady state and transient state experiments are made with different machine speeds. During the tests, the field current is fixed at 2A and the IGBT gate drive supply voltage is 60V.

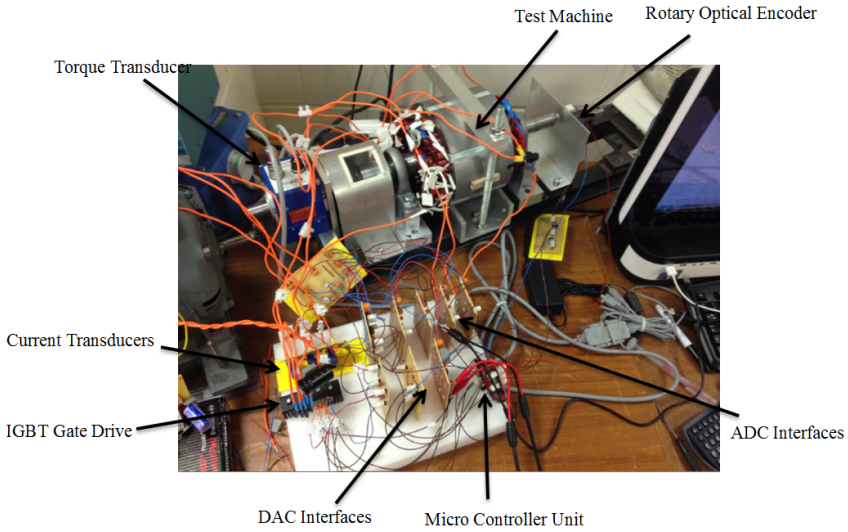

Fig. 7: Experiment set-up

All the terminal measurements are input via appropriate ADC interfaces to the micro-controller for arithmetic processing. Quantities within the micro-controller are normalised to a p.u. system within a range of -1 to +1. Desired waveforms are output from DAC pins of the micro-controller and picked up by oscilloscope probes via the DAC interfaces. Voltage output range of DAC pins is -3.3V to +3.3V. An optical rotary encoder provides the actual q-axis position and instantaneous rotor speed, as a reference to estimations.

It is shown that the estimations of $e_{S\alpha}$ and $e_{S\beta}$ are essential to the scheme. The estimated waveforms of $e_{S\alpha}$ and $e_{S\beta}$ at two different machine speeds are recorded in Fig. 8.

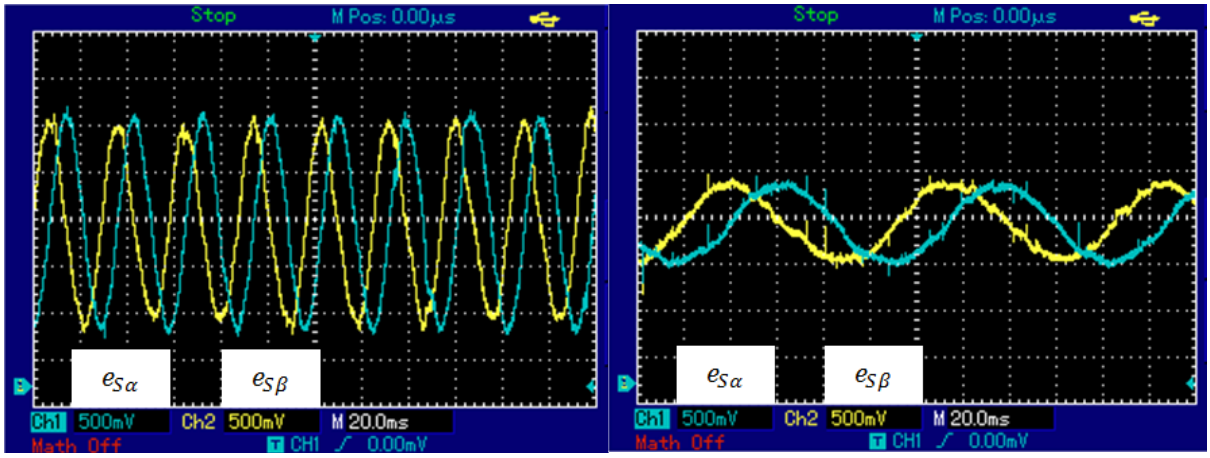

(a) (b)

Fig. 8: Waveforms of $e_{S\alpha}$ and $e_{S\beta}$ at (a) 500rpm and (b) 150rpm

The estimated and reference q-axis positions when the machine is running without load at 2 different speeds are compared in Fig. 9, with the estimation error highlighted. It is seen that the waveforms of estimated (yellow) and reference (blue) q-axis are almost indistinguishable under both speeds at no load. The spikes appearing on the error waveforms are due to the transitions from 2π to 0 of the position saw tooth waveforms. Generally the estimation error is generally well below 5% of the waveform amplitude.

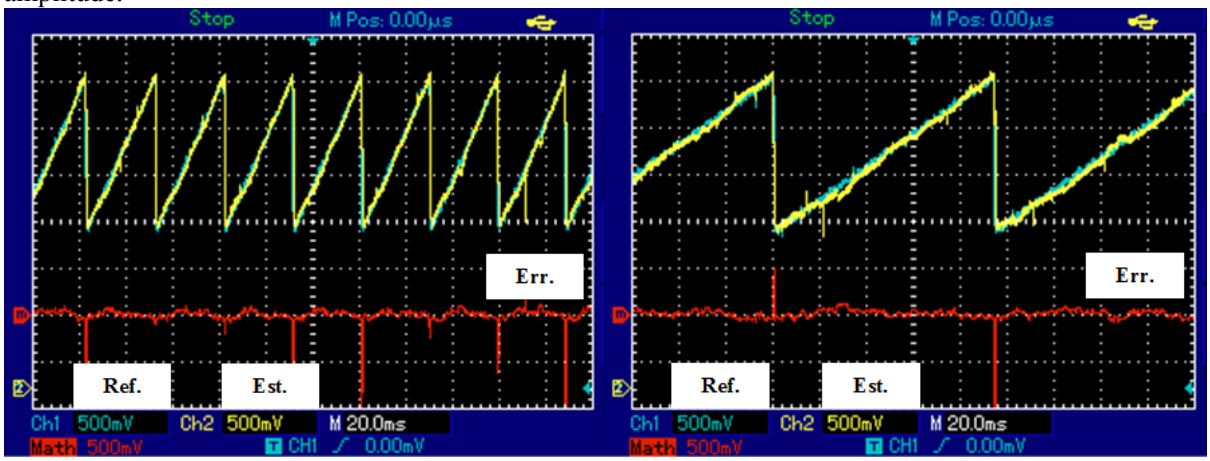

(a) (b)

Fig. 9: Q-axis position estimation performances at (a) 500rpm and (b) 150rpm, with no load

Figure 10 shows the estimated and reference q-axis positions when the machine is loaded (i_q=0.5p.u.). The estimation error at high speed (500rpm) is not distinctly affected by loading, while the estimation error at low speed (150rpm) is increased when the machine is under load. It is because that the armature resistive voltage drop at high machine speed is negligible compared with the internal emf, while it becomes influential and non-negligible in the case of low machine speed.

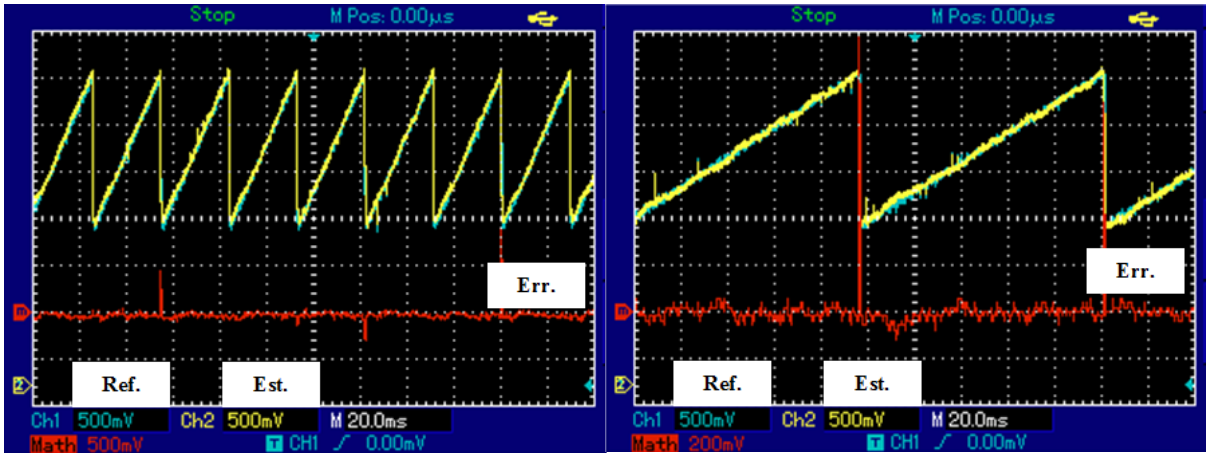

(a) (b)

Fig. 10: Q-axis position estimation performances at (a) 500rpm and (b) 150rpm, with load

Figure 11 evaluates the position estimation when the test machine experiences a sudden loading (i_q=0.5p.u.). It is observed that the sudden loading influences the estimation performance at both machine speeds, and its influence at low speed is more considerable. Even through, the position error is still within acceptable range and it decays at the machine transitions from transient state to steady state.

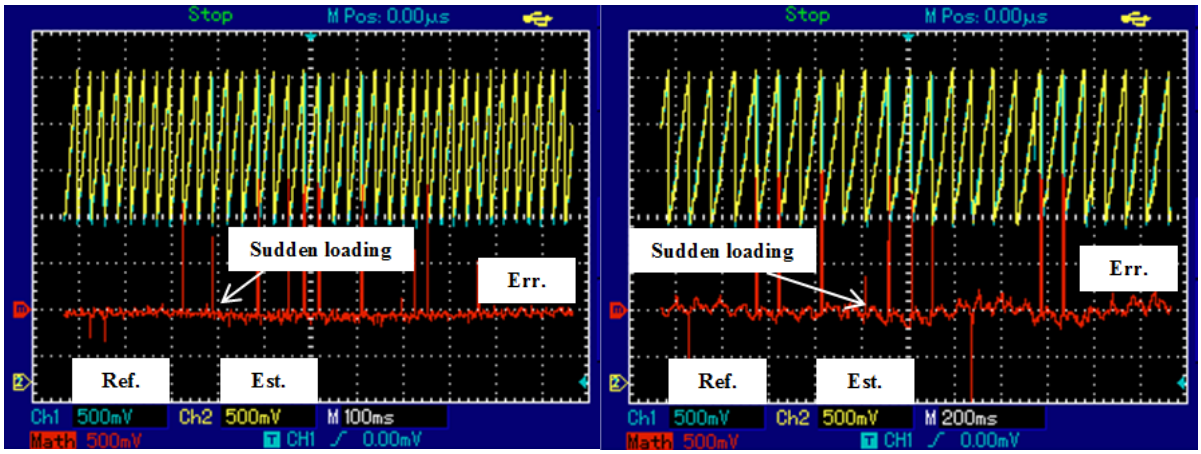

(a) (b)

Fig. 11: Q-axis position estimation performances at (a) 500rpm and (b) 150rpm, with transient load

Steady state speed estimation performance is evaluated in Fig. 12 with three speed steps. The speed estimation exhibits good correspondence with reference speed (i.e. actual speed) even at low speed range.

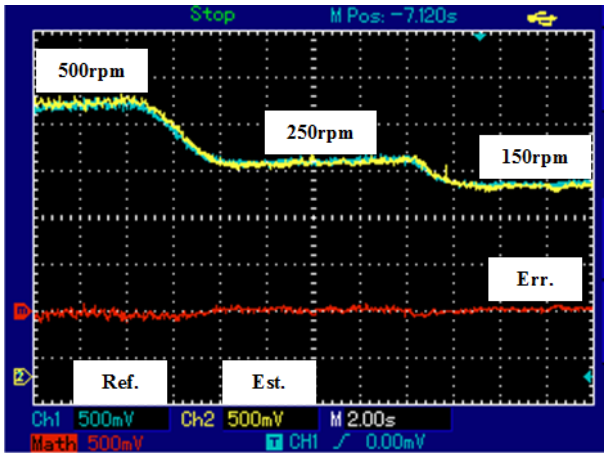

Fig. 12: Rotor speed estimation performance at steady state

The transient speed estimation test is performed when a considerable sudden external torque is applied to the test machine and causes a substantial drop of machine speed. The situations of both high and low speeds are measured on the test machine and are shown in Fig.13.

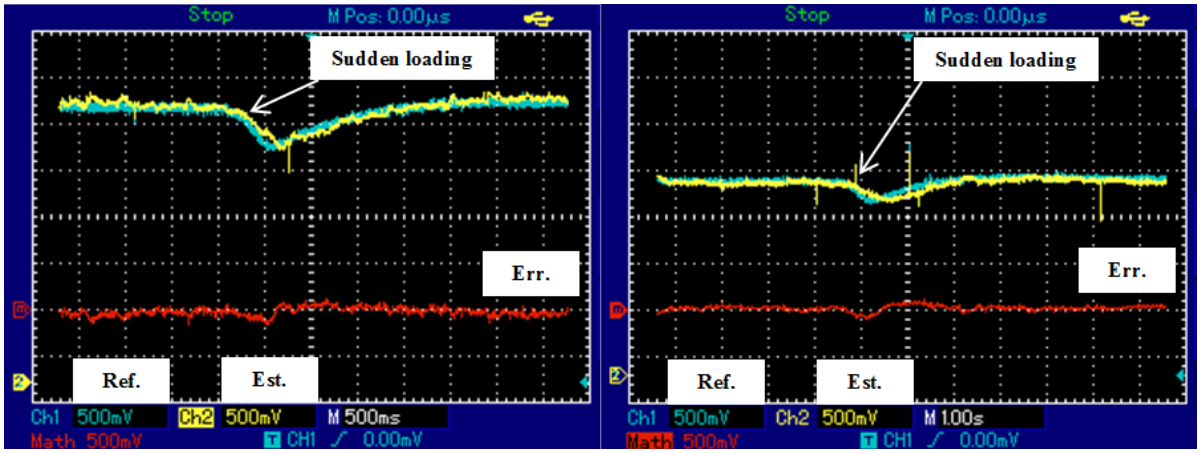

(a) (b)

Fig. 13: Rotor speed estimation performance at (a) 500rpm and (b) 150rpm, with transient load

In both cases, the speed estimator manages to record the speed dip due to the sudden loading. However, there is an obvious lag of estimated speed response during the transient compared with the actual speed response. It is due to the time delay introduced by the moving average filter. The amount of lag is determined by the time constant of the filter. This could be reduced with another design of filter.

Conclusion

This paper proposes a novel sensorless position and speed estimation method for heteropolar inductor machines based on their structural advantages, since the field windings are placed on stator side. The characteristics of flux linkages and induced voltages in field windings reveal the potential possibility to exact position information. The mathematics of developing the sensorless strategy is introduced based on machine's space vector model. The estimation theories under both steady and transient states are validated in practice. Both q-axis position and rotor speed estimations are proven to be acceptable compared with practical measurements. The error of q-axis estimation is generally kept within 10% and the influence of loading is minimized if the machine is operating at a high speed. The rotor speed estimation is satisfactory except for possible response delays introduced by filtering.

References

[1] Z. Q. Zhu and J. T. Chen, "Advanced Flux-Switching Permanent Magnet Brushless Machines," *Magnetics, IEEE Transactions on,* vol. 46, pp. 1447-1453, 2010.

[2] C. Pollock and M. Wallace, "The flux switching motor, a DC motor without magnets or brushes," in *Industry Applications Conference, 1999. Thirty-Fourth IAS Annual Meeting. Conference Record of the 1999 IEEE*, 1999, pp. 1980-1987 vol.3.

[3] W. Jingzhe and M. J. Balchin, "Analysis of heteropolar inductor machines based on space vectors," in *Electric Power and Energy Conversion Systems (EPECS), 2013 3rd International Conference on*, 2013, pp. 1-6.

[4] W. Leonhard, *Control of Electrical Drives*: Springer Berlin Heidelberg, 2001.

[5] G. S. Buja and M. P. Kazmierkowski, "Direct torque control of PWM inverter-fed AC motors - a survey," *Industrial Electronics, IEEE Transactions on,* vol. 51, pp. 744-757, 2004.

[6] W. Yu, D. Zhiquan, and W. Xiaolin, "A Parallel Hybrid Excitation Flux-Switching Generator DC Power System Based on Direct Torque Linear Control," *Energy Conversion, IEEE Transactions on,* vol. 27, pp. 308-317, 2012.

[7] K. Wang, J. X. Shen, and S. Z. Dong, "Sensorless control and initial position estimation of permanent magnet flux switching motor," in *Electrical Machines and Systems, 2007. ICEMS. International Conference on*, 2007, pp. 487-491.

[8] W. Yu and D. Zhi-Quan, "A Position Sensorless Method for Direct Torque Control With Space Vector Modulation of Hybrid Excitation Flux-Switching Generator," *Energy Conversion, IEEE Transactions on,* vol. 27, pp. 912-921, 2012.

[9] J. H. Walker, "The theory of the inductor alternator," *Electrical Engineers - Part II: Power Engineering, Journal of the Institution of,* vol. 89, pp. 227-241, 1942.